Quasi-2D Heisenberg antiferromagnets $[CuX(pyz)_2](BF_4)$ with X = Cl and Br

Mariusz Kubus[†‡], Arianna Lanza[†§], Rebecca Scatena[†], Leonardo H. R. Dos Santos[†], Björn Wehinger[‡#], Nicola Casati[§], Christoph Fiolka[†], Lukas Keller[‡], Piero Macchi[†]*, Christian Rüegg[‡#]*, Karl W. Krämer[†]*

[†]Department of Chemistry and Biochemistry, University of Bern, Freiestrasse 3, CH-3012 Bern, Switzerland

[‡]Laboratory for Neutron Scattering and Imaging, Paul Scherrer Institute, CH–5232 Villigen PSI, Switzerland

[§]Laboratory for Synchrotron Radiation – Condensed Matter, Paul Scherrer Institute, CH–5232 Villigen PSI, Switzerland

[#]Department of Quantum Matter Physics, University of Geneva, Quai Ernest Ansermet 24, CH-1211 Genève 4, Switzerland

ABSTRACT: Two Cu^{2+} coordination polymers $[CuCl(pyz)_2](BF_4)$ **1** and $[CuBr(pyz)_2](BF_4)$ **2** (pyz = pyrazine) were synthesized in the family of quasi two-dimensional (2D) $[Cu(pyz)_2]^{2+}$ magnetic networks. The layer connectivity by mono-atomic halide ligands is novel and results in significantly shorter interlayer distances. Structures were determined by single crystal X-ray diffraction. The isostructural compounds crystallize in the tetragonal space group $P4/nbm$. $[Cu(pyz)_2]^{2+}$ layers are connected by halide ions along the *c*-axis and charge is compensated by BF_4^- ions located in the voids of the 3D coordination network. Temperature dependent X-ray diffraction of **1** revealed the rigidity of the $[Cu(pyz)_2]^{2+}$ layers which do not expand between 5 K and room temperature, whereas the expansion along the *c*-axis amounts to 2 %. The magnetic susceptibility of **1** and **2** shows a broad maximum around 8 K, indicating quasi 2D antiferromagnetic interactions within the $[Cu(pyz)_2]^{2+}$ layers. 2D Heisenberg model fits result in $J_{||}$ = 9.4(1) K for **1** and 8.9(1) K for **2**. The inter-layer coupling is much weaker with $|J_{\perp}|$ = 0.31(6) K for **1** and 0.52(9) K for **2**. The electron density, experimentally determined and calculated by density functional theory, confirm the location of the singly occupied orbital (the magnetic orbital) in the tetragonal plane. The analysis of the spin density reveals a mainly σ-type exchange through the pyrazine. Kinks in the magnetic susceptibility indicate the onset of long-range 3D magnetic order below 4 K. The magnetic structures were determined by neutron diffraction. Magnetic Bragg peaks occur below T_N = 3.9(1) K for **1** and 3.8(1) K for **2**. The magnetic unit cell is doubled along the *c*-axis ($\boldsymbol{k}$ = 0, 0, 0.5). The ordered magnetic moments are located in the tetragonal plane and amount to 0.76(8) μ_B/Cu^{2+} for **1** and 0.6(1) μ_B/Cu^{2+} for **2** at 1.5 K. The moments are coupled antiferromagnetically both in the *a*-*b* plane and along the *c*-axis. The anisotropy of the Cu^{2+} *g*-tensor was determined from powder and single crystal ESR spectra as g_x = 2.060(1), g_z = 2.275(1) for **1** and g_x = 2.057(1), g_z = 2.272(1) for **2** at room temperature.

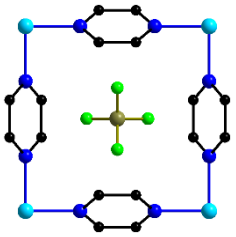

INTRODUCTION

Quasi two-dimensional (2D) S=1/2 square-lattice Heisenberg antiferromagnets (AFM) have attracted much attention in recent years as magnetic model systems due to their relation to high T_C cuprate superconductors,[1,2,3] their quantum fluctuations below T_N, and a possible application in quantum computing.[4,5,6] Molecular magnets play a major role in this field.[7,8,9] Their versatile composition from metal ions as spin carriers and ligands as linkers allows the design of tailored lattices for magnetic model systems.[10,11] Composition, configuration geometry, and conjugation of the linkers influence the exchange between magnetic centers. Often studied are systems with short linkers, e.g. O^{2-}, OH^-, N^{3-}, or conjugated groups, such as oxalate or pyrazine (pyz).[10,12] The search for new magnetic materials for experimental and theoretical investigations can be based on modifications of known compounds, e.g. the single and double layer models $[CuF_2(H_2O)_2(pyz)]$[13] and $[(CuF_2(H_2O)_2)_2(pyz)]$[14], respectively, or the exploration of new systems. Cu^{2+} ions with their small *S*=1/2 spin are of particular interest in quantum magnetism. Coordination compounds are rather soft and susceptible to the application of external pressure which may induce structural or magnetic phase transitions.[15] The relatively weak magnetic interactions in these 2D Cu^{2+} materials result in moderate

saturation fields at low temperature[16] which are experimentally accessible and allow a direct determination of the coupling parameters by inelastic neutron scattering.

The family of $[CuX(pyz)_2]Y$ compounds has attracted major attention in this field. These compounds are based on $[Cu(pyz)_2]^{2+}$ layers which are bridged in the third dimension by X ligands and charge is compensated by Y anions. Their 3D coordination network hosts quasi 2D magnetic interactions. As examples, X can be NO_3^- and Y = PF_6^- [16], or X = HF_2^- and Y = ClO_4^- [4], BF_4^- [17], PF_6^- [4], SbF_6^- [18], AsF_6^- [4], or TaF_6^- [19].

Data available in literature do not allow an easy rationalization of the magnetic exchange in this family of compounds. In particular, the role of interlayer interactions through X anions or the role of the counter-ion Y remain unclear. For this reason, we synthesized new compounds and characterized their structure/property relationships. Here, we present two new members of the $[CuX(pyz)_2]Y$ family $[CuCl(pyz)_2](BF_4)$ **1** and $[CuBr(pyz)_2](BF_4)$ **2** with a novel mono-atomic connectivity between the layers by halide ions. Syntheses and crystal growth are discussed. The crystal and magnetic structures were determined by X-ray and neutron diffraction. The experimental electron density distribution is compared to the density functional theory one. The magnetic properties were determined by SQUID and ESR measurements and discussed in the $[Cu(pyz)_2]^{2+}$ series.

EXPERIMENTAL SECTION

Synthesis. The title compounds were obtained *via* two synthetic routes.

Method 1: $[CuCl(pyz)_2](BF_4)$, **1**, was crystallized from a solution of stoichiometric amounts of 4.9894 g $Cu(BF_4)_2{\cdot}6H_2O$ (Alfa Aesar, 98%), 0.7730 g NH_4Cl (Merck, 99.8%), and 2.3148 g pyrazine (Acros, 99+%) in 0.5 l water according to reaction (1). The mixture was cooled until **1** precipitated (yield 32%).

$$Cu(BF_4)_2 + NH_4Cl + 2\ pyz \rightarrow [CuCl(pyz)_2](BF_4) + NH_4BF_4 \quad (1)$$

Method 2: $[CuCl(pyz)_2](BF_4)$, **1**, was obtained from an aqueous solution of 1.9431 g $CuCl_2$ (Aldrich, ≥99.995%), 2.8134 g $Ag(BF_4)$ (Strem, 99%), and 2.3148 g pyrazine (Acros, 99+%) according to reaction (2). First, $CuCl_2$ was dissolved in 250 ml H_2O and $Ag(BF_4)$ was added. After 30 min. of stirring, the precipitated AgCl was filtered off. Then the pyrazine dissolved in 250 ml water was slowly added. The mixture was cooled until precipitation occurred (yield 60%). Upon slow evaporation at 5 °C during a few weeks, dark blue crystals with a tetragonal prismatic habitus were obtained.

$$CuCl_2 + Ag(BF_4) + 2\ pyz \rightarrow [CuCl(pyz)_2](BF_4) + AgCl \quad (2)$$

$[CuBr(pyz)_2](BF_4)$, **2**, was synthetized according to method 2 from $CuBr_2$ (Aldrich, 99.999%).

For powder neutron diffraction measurements deuterated samples were prepared. They were synthesized from deuterated pyrazine (D_4-pyz, CIL, >98% D) and D_2O (ARMAR, 99.8% D). The samples were dried for one hour in vacuum at room temperature.

Characterization. The thermal stability range of the compounds was determined on a Mettler Toledo TGA/SDTA851 thermo-balance. Samples of about 20 mg weight were heated by 5 K/min. in corundum crucibles in a N_2 gas flow of 20 ml/min. The TGA curves are shown in Figure 1S of the supporting information (SI).

Table 1. High resolution crystal data and structure refinement of $[CuCl(pyz)_2](BF_4)$ 1 and $[CuBr(pyz)_2](BF_4)$ 2 at 100 K.

Empirical formula	$[CuCl(pyz)_2](BF_4)$	$[CuBr(pyz)_2](BF_4)$
Formula weight / g mol^{-1}	345.98	390.45
Temperature / K	100(2)	100(2)
Crystal system	tetragonal	tetragonal
Space group	*P4/nbm* (125)	*P4/nbm* (125)
a, *b* / Å	9.74670(10)	9.75710(10)
c / Å	5.61790(10)	5.84500(10)
Volume / Å^3	533.690(14)	556.450(15)
Z	2	2
ρ_{calc} / g cm^{-3}	2.153	2.330
μ / mm^{-1}	2.341	5.595
F(000)	342	378
2Θ range /°	5.9 - 105.3	5.9 - 91.2
Index ranges	-21 ≤ h ≤ 21 -21 ≤ k ≤ 21 -12 ≤ l ≤ 12	-19 ≤ h ≤ 19 -19 ≤ k ≤ 19 -11 ≤ l ≤ 11
collected/independent reflections	31788 / 1655	39145 / 1252
R_{int}	0.017	0.027
R_σ	0.005	0.007
Spherical atom refinement		
Data/restraints/parameters	1655/0/32	1252/0/27
Goodness-of-fit on F^2	1.145	1.115
Final R indexes [I≥2σ (I)]	R_1 = 0.016, wR_2 = 0.05	R_1 = 0.017, wR_2 = 0.04
Final R indexes [all data]	R_1 = 0.017, wR_2 = 0.05	R_1 = 0.022, wR_2 = 0.04
Largest diff. peak/hole / e Å^{-3}	0.65/-0.69	0.64/-0.52
Multipole model refinement		
Data/restraints/parameters	1655/5/105	1252/5/103
Final R indexes [all data]	R_1 = 0.011 wR_2 = 0.02	R_1 = 0.019 wR_2 = 0.02
Largest diff. peak/hole / e Å^{-3}	0.28/-0.25	0.33/-0.32

Fourier transform infrared (FTIR) spectra were measured on a JASCO FT/IR-4700 spectrometer. A FTIR spectrum of **1** is shown in Figure 2S of SI.

Single crystal X-ray diffraction. Crystals were mounted with grease on a glass fiber and cooled by an Oxford cryostream N_2 flow cryostat. Preliminary measurements were carried out at 173(2)K up to a resolution of 0.67 Å, whereas extensive high resolution data collections (d_{min} = 0.45 Å) were carried out at 100(2)K, for $[CuCl(pyz)_2](BF_4)$, $[CuCl(D_4\text{-}pyz)_2](BF_4)$, and $[CuBr(pyz)_2](BF_4)$. All measurements were made on an Oxford Diffraction SuperNova area-detector diffractometer using mirror optics, monochromated, and Al filtered[20] microsource Mo K_α radiation (λ = 0.71073 Å). Data reduction was performed using the CrysalisPro program.[21] The intensities were analytically corrected for Lorentz and polarization effects and for absorption with the Gaussian method based on the crystal shape. The pyrazine H-atoms were placed in positions calculated theoretically and refined using a riding model. Selected crystallographic data and structural refinement details are summarized in Table 1. Atomic positions and equivalent isotropic displacement parameters are given in Table 2S of SI.

The conventional structural refinements were carried out using SHELXL.[22] The multipole refinements with the Hansen-Coppens formalism[23] for accurate charge density determination were performed using XD2015.[24] More details on the multipolar models are given in the SI. The highest and lowest residual density peaks were 0.28 and -0.25 eÅ^{-3} for **1** and 0.33 and -0.32 eÅ^{-3} for **2** using in both cases all the data. Residual density maps show only small and random discrepancies.

The *d*-orbital occupancies were derived with the assumption of low *sp* to *d* overlap, according to the approach suggested by Holladay, Leung, and Coppens[25] using the XDPROP module. Topological properties and integrated atomic charges were calculated using the TOPXD module.

Powder X-ray diffraction. Powder X-ray diffraction patterns were measured on a STOE STADIP diffractometer in Debye-Scherrer geometry at room temperature. Samples were prepared on thin plastic foil. Diffraction patterns were measured with Cu $K_{\alpha 1}$ radiation (λ = 1.54059 Å) from a focusing Ge (111) monochromator and recorded with a position sensitive Mythen 1K detector with 0.01° resolution in 2-Theta.

Low temperature X-ray diffraction patterns were measured at the powder diffraction station of the Swiss Light Source at the Paul Scherrer Institute (PSI).[26] The sample was filled in a 0.3 mm capillary and cooled in a He flow cryostat. Data were measured between 5 and 290 K at a wavelength of λ = 0.56496 Å. The T dependent unit-cell parameters were refined with Topas Academic.[27]

Powder neutron diffraction. Powder diffraction patterns were measured on the cold neutron diffractometer DMC[28] of the Swiss spallation neutron source at PSI. Powder samples of 3 g deuterated $[CuX(D_4\text{-}pyz)_2](BF_4)$ with X = Cl and Br were sealed in V cans under He gas. Neutrons with wavelengths of λ = 4.5040 Å and 3.8040 Å were used. The samples were cooled in an ILL-type He cryostat with a base temperature of 1.5 K.

Powder diffraction data were analyzed with the FullProf program package.[29,30]

Magnetic measurements. Magnetic susceptibility data were recorded on a Quantum design MPMS-5XL SQUID magnetometer in the temperature range from 1.9 to 300 K and a magnetic field of 0.2 Tesla for a crystal and deuterated powder of **1**, 0.1 Tesla for a powder of **2**, and 0.05 Tesla for a powder of **1**. Magnetization measurements were done at 1.9 K in fields up to 5 Tesla. Susceptibility data were corrected for diamagnetic contributions from the sample ($-0.45\cdot10^{-6}$ cm^3/g · molar weight), the empty sample holder, and the temperature independent paramagnetic contribution of Cu^{2+}.

ESR spectroscopy. ESR spectra of powder and crystal samples were recorded on a Bruker E-500 spectrometer in the X-band at room temperature.

Electronic structure calculations. Periodic Density Functional Theory calculations were carried out using the software CRYSTAL14.[31] The functional B3LYP was used with basis set 86-411G(41d)[32] for the Cu and pob-TZVP[33] for all the other atoms. The theoretical electron density was analyzed with the TOPOND module of CRYSTAL14. Selected crystal dimeric/tetrameric units were calculated with GAUSSIAN09[34] using again the B3LYP functional and the basis set 6-311G(2d,2p). More details about the dimeric/tetrameric units are given in the SI.

Table 2. Atomic distances (Å) and angles (°) of $[CuCl(pyz)_2](BF_4)$, 1, and $[CuBr(pyz)_2](BF_4)$, 2, at 100 K.

	$[CuCl(pyz)_2](BF_4)$	$[CuBr(pyz)_2](BF_4)$
Cu-N (4×)	2.0544(3)	2.0559(5)
Cu-X (2×)	2.8089(1)	2.9225(1)
pyz rotation angle	58.35(2)	55.01(3)
Cu-Cu distances		
Cu-pyz-Cu (=|**a**+**b**|/2)	6.8920(1)	6.8993(1)
Cu-X-Cu (= |**c**|)	5.6179(1)	5.8450(1)

Table 3. Structural and magnetic parameters of compounds with tetragonal $[Cu(pyz)_2]^{2+}$ layers. The pyz rotation angle is the deviation from the tetragonal layer. All data at room temperature, except for No. 5 at 163 K.

No.	Compound	Space group	Distance (Å)		Cu-Cu Distance (Å)		pyz rot. angle (°)	$J_{\|\|}$ (K)	T_N (K)	Ref.
			Cu-N	Cu-X	Cu-pyz-Cu	Cu-X-Cu				
1	$[Cu(HF_2)(pyz)_2](SbF_6)$	*P*4/*nmm*	2.048	2.338	6.876	6.97	81.4	13.4	4.3	[18][a)]
2	$[Cu(HF_2)(pyz)_2](TaF_6)$	*P*4/*mmm*	2.047	2.367	6.862	7.027	90.0	13.1	4.2	[19][b)]
3	$[Cu(HF_2)(pyz)_2](AsF_6)$	*P*4/*mmm*	2.046	2.333	6.865	6.950	90.0	12.8	4.3	[4]
4	$[Cu(HF_2)(pyz)_2](PF_6)$	*P*4/*mmm*	2.041	2.312	6.854	6.893	90.0	12.4	4.3	[4,35]
5	$[Cu(NO_3)(pyz)_2](PF_6)$	*I*4/*mcm*	2.042	2.413	6.866	7.003	61.4	10.8	2.0	[16,36][c)]
6	$[CuCl(pyz)_2](BF_4)$, **1**	*P*4/*nbm*	2.053	2.865	6.895	5.731	58.8	9.4	3.9	this work
7	$[CuBr(pyz)_2](BF_4)$, **2**	*P*4/*nbm*	2.052	2.963	6.894	5.926	55.4	8.9	3.8	this work
8	$[Cu(NO_2)(pyz)_2](ClO_4)$	*P*4/*nbm*	2.049	2.285	6.877	6.646	59.8	8.9	N/A	[37]
9	$[Cu(HF_2)(pyz)_2](ClO_4)$	*P*4/*nbm*	2.040	2.228	6.863	6.689	64.2	7.3	1.9	[4]
10	$[Cu(HF_2)(pyz)_2](BF_4)$	*P*4/*nbm*	2.039	2.208	6.852	6.619	59.4	6.3	1.5	[4,17,38]

a) [4] reports space group *P*4/*mmm* and 90° pyz rotation angle at room temperature. At 90 K, the pyz rotation angle is 79.1°.

b) At 90 K, the space group is *P*4/*nmm* with a pyz rotation angle of 79.5°.

c) The structure is highly disordered.

RESULTS AND DISCUSSION

$[CuCl(pyz)_2](BF_4)$, **1**, and $[CuBr(pyz)_2](BF_4)$, **2**, are isostructural and crystalize in the tetragonal space group *P*4/*nbm*, see Figure 1. Room temperature powder diffraction pattern and Rietveld fits, see Figures 3S - 4S of SI, demonstrate the phase purity of the samples and they perfectly agree with single crystal data. In these structures, the Cu^{2+} ions have a distorted octahedral coordination by four N atoms from pyrazine in the tetragonal plane and by two halide anions along the *c*-axis. The Cu-N distances of 2.054 Å and 2.056 Å are rather close, whereas the Jahn-Teller distorted Cu-X distances increase from 2.809 Å (**1**) to 2.923 Å (**2**), see Table 2. Both the pyrazine and the halide ligands act as bidentate linkers connecting Cu^{2+} ions into a 3D coordination network. The pyz rings are rotated around the Cu-N-N-Cu axis by 58.4° (**1**) and 55.0° (**2**) from the tetragonal plane. The BF_4^- anions occupy voids in the 3D network and are linked by F···H bonds to pyz molecules.

The 3D structural network explains some of the chemical properties of these compounds. They have a rather low solubility in water and rapidly precipitate as powder, which hardly re-dissolves. Single crystals of mm size and tetragonal prismatic habitus grew by slow evaporation over several weeks at 5°C. The 3D coordination network gives rise to high thermal stability. **1** and **2** decompose in a one-step process above 240°C and 227°C, respectively, see the TG curves in Figure 1S of SI. The decomposition product is the respective monovalent copper halide CuX with X = Cl, Br, as confirmed by powder X-ray diffraction.

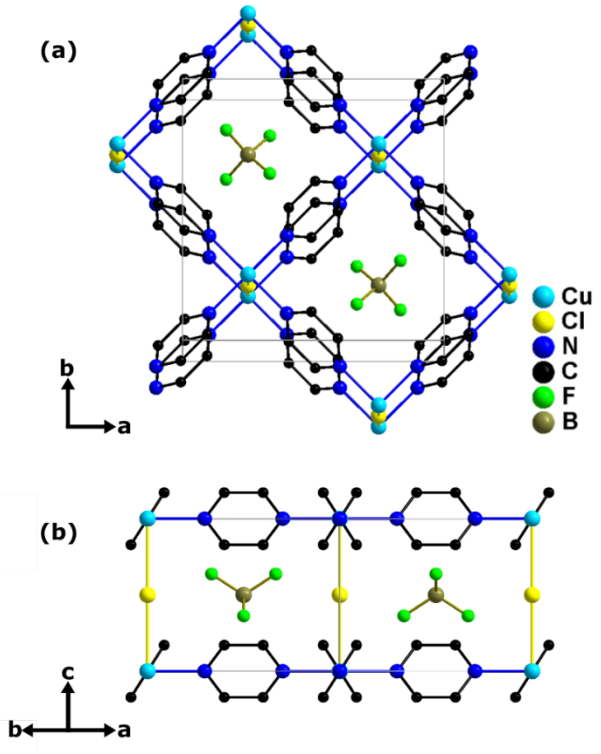

Figure 1. View onto the crystal structure of $[CuCl(pyz)_2](BF_4)$ (a) along the *c*-axis and (b) along [110]. Hydrogen atoms are omitted for clarity. The unit cell is outlined by grey lines.

Temperature dependent powder X-ray diffraction measurements provided information on the thermal expansion of $[CuCl(pyz)_2](BF_4)$. The relative change of lattice parameters and molar volume is shown in Figure 2 and more details are given in Table 1S of SI. The thermal lattice expansion is very anisotropic. Along the *a*-axis (=*b*) one observes even a slight contraction $\Delta a/a$ = -0.1% whereas along the *c*-axis the lattice strongly expands by $\Delta c/c$ = 2.1%. The molar volume increases by 1.9% from 160.44(1) to 163.63(1) cm^3/mol between 5 K and 290 K. These results demonstrate the extraordinary rigidity of the $[Cu(pyz)_2]^{2+}$ layers and the softness of the Jahn-Teller distorted Cu-X-Cu bonds within the 3D coordination network.

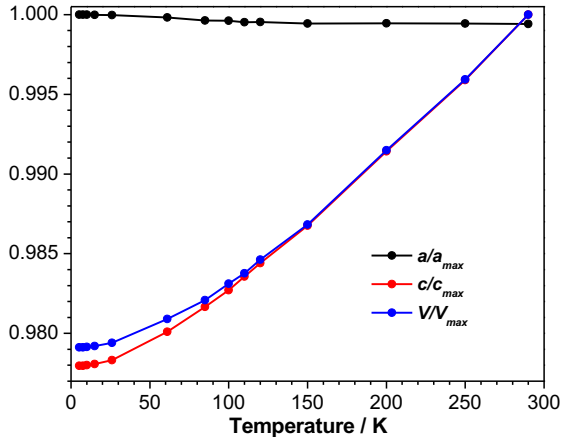

Figure 2. Temperature dependence of the reduced lattice parameters and molar volume of $[CuCl(pyz)_2](BF_4)$. The lines are a guide to the eye.

The crystal structures of **1** and **2** are closely related to $[Cu(HF_2)(pyz)_2]Y$ with Y = ClO_4^-, PF_6^-, SbF_6^-, AsF_6^-, or TaF_6, see Table 3. All these tetragonal compounds contain $[Cu(pyz)_2]^{2+}$ layers as their characteristic structural feature. Further related compounds with distorted $[Cu(pyz)_2]^{2+}$ square nets, e.g. $[Cu(ClO_4)_2(pyz)_2]$ and $[Cu(pyz)_2(NO_3)]NO_3{\cdot}H_2O$, are summarized in Table 3S of SI. In $[Cu(pyz)]^{2+}$ compounds, the angle between the tetragonal plane and the pyz ring is close to 90° for bigger octahedral Y anions, or close to 60° for smaller tetrahedral anions; the only exception is Y = PF_6^- which gives both, depending on the interlayer linker, see Table 3. We note however, when low T measurements are available, all structures have a pyrazine rotation angle smaller than 90°. Some structures at room temperature have been refined in *P*4/*mmm*,[4,19,34] therefore with pyz necessarily orthogonal to the tetragonal layer. However, a careful inspection of atomic displacement parameters of pyz C atoms in these structures reveals that these are compatible with a disorder between two orientations of the pyrazine ring and therefore the reported 90° angles are deceptive.

In the $[CuX(pyz)_2](BF_4)$ compounds **1** and **2**, the layers are linked by mono-atomic halide ligands, which is unprecedented for the $[Cu(pyz)]^{2+}$ structural family. For all other compounds, the connection occurs via polyatomic anions, such as FHF^-, NO_2^-, or NO_3^-, as well as BF_4^- and ClO_4^- for the distorted square nets. Accordingly, **1** and **2** show the by far shortest interlayer Cu-X-Cu distances, which are significantly shorter than the intralayer Cu-pyz-Cu distances, see Table 2.

The Cu-ligand distances in $[CuX(pyz)_2](BF_4)$ indicate that the elongated Jahn-Teller axis is located parallel to the *c*-axis and therefore the unpaired electron of the $d_{x^2-y^2}$ orbital localized in the *a*-*b* plane. As local coordinate system for the Cu^{2+} ion, we adopt $x = \boldsymbol{a}+\boldsymbol{b}$, $y = \boldsymbol{a}-\boldsymbol{b}$, $z = \boldsymbol{c}$. Therefore, the magnetic interactions predominantly occur within the $[Cu(pyz)_2]^{2+}$ layers of the *a*-*b* plane, resulting in a quasi 2D magnetic network, despite the 3D nature of the coordination network and the shorter interlayer Cu-X-Cu distances.

If the Cu-pyz direction was instead Jahn-Teller distorted, the Cu-N distances would be about 2.40 Å, see for example Ref. [14], which is distinctly longer than the observed distances reported in Table 2.

Table 4. d-electron populations from experimental multipolar refinements (exp. MM), multipolar refinements of theoretical calculations (calc. MM), and periodic DFT calculations (calc.).

	$d_{x^2-y^2}$	d_{xz}	d_{xy}	d_{yz}	d_{z^2}
$[CuCl(pyz)_2](BF_4)$, **1**					
exp. MM	1.644(3)	2.102(2)	1.996(3)	2.102(2)	2.196(4)
calc. MM	1.609	2.120	2.114	2.120	2.123
calc.	1.393	1.981	1.977	1.981	1.986
$[CuBr(pyz)_2](BF_4)$, **2**					
exp. MM	1.631(5)	2.099(4)	2.091(5)	2.099(4)	2.068(6)
calc. MM	1.610	2.128	2.088	2.128	2.135
calc.	1.393	1.980	1.978	1.980	1.985

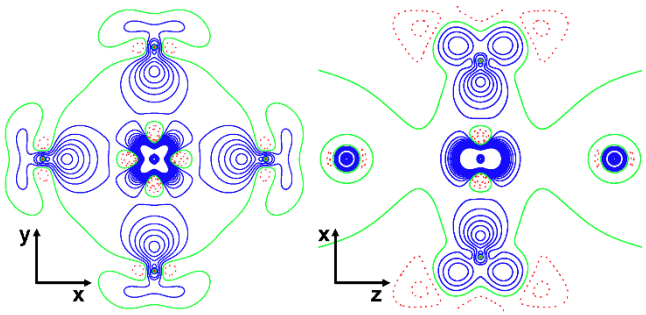

Figure 3. Static deformation electron density maps of **1**. The x-y and x-z planes (in the local Cu^{2+} coordinate system) are depicted. Blue and red contours (0.2 e/Å^3), respectively, represent the excess and depletion of electron density with respect to the spherical atom distribution. The green contour is the zero level.

From high resolution single crystal X-ray diffraction experiments at 100 K and periodic DFT calculations the electron density distribution in both compounds was determined. The coefficients of the experimental multipolar refinement were converted into occupancies of the *d*-orbitals.[25] In agreement with periodic DFT calculations, the electron population of the $d_{x^2-y^2}$ orbital is distinctly smaller than for all other *d* orbitals, see Table 4. This result confirms that $d_{x^2-y^2}$ is, in a first approximation, the single-occupied, magnetic orbital. It is generally observed that the experimental multipole refinements exceed the occupation of 2.0 for fully occupied orbitals, see for example Ref. [39]. These parameters were freely refined without a constraint and represent *d*-shaped electron density functions, not directly *3d*-orbitals. A comparison with multipole refinements fitted to theoretical data (DFT) is very useful, see Table 4, indicating a good agreement between theory and experiments, when the same multipolar expansion is applied. The experimental deformation density maps clearly confirm the charge depletion of the Cu^{2+} ion along the *x* and *y* directions in the local coordinate system, see Figure 3.

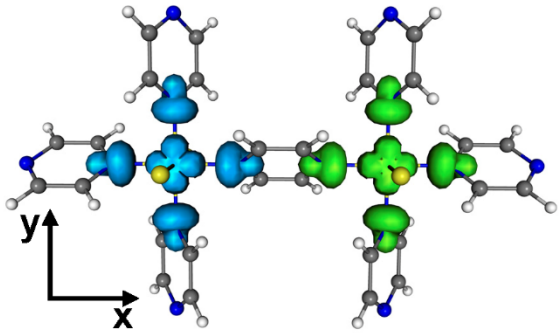

Figure 4. The calculated spin density distribution imposes an antiferromagnetic coupling in the [Cu2Cl4(pyz)7] dimer. Cyan and green surfaces represent excess and defect of α spin density at values ±0.013 eÅ^{-3}.

The topological analysis of the experimental and theoretical electron densities, through quantum theory of atoms in molecules (QTAIM),[40] enables addressing the main bonding features in the two structures, see Table 4S of SI. In particular, we focus the attention on bonds to Cu and electron sharing, including delocalization between atoms not directly connected by a bond path. The electron delocalization indices cannot be derived from the experimental electron density, but they are computed from gas phase calculations on a dimeric $[Cu_2X_4(pyz)_7]$ unit.

In general, the two compounds show very similar features, both in the experimental and the theoretical analysis. The electron density calculated at the bond critical points of Cu-X bonds is ca. 1/3 that of Cu-N bonds. Similarly, the electron delocalization indices of Cu-X bonds are ca. 1/2 of Cu-N bonds. This mainly reflects the Jahn-Teller distortion and the lower (though not-negligible) electron sharing occurring along this coordination direction. The 1,3 C-C and C-N interactions in the pyrazine ring have an electron delocalization of ca. 0.1 electron pairs due to the large resonance within the aromatic ligand. Of course, the 1,2 interactions have a much larger delocalization of ca. 1.3 electron pairs. Instead, the 1,3 Cu-C interaction is much weaker (< 0.02 electron pairs). This confirms the previous suggestion that a π driven Cu-Cu magnetic exchange through the pyrazine is not favorable; this would be possible only through a significant Cu-C exchange, which does not occur, see e.g. the discussion in Ref. [38]. The Cu-N interaction cannot provide any contribution to a π driven Cu-Cu magnetic exchange, because the atomic orbitals p_z

of N and $d_{x^2-y^2}$ of Cu are necessarily orthogonal to each other. Accordingly, the large Cu-N exchange can only contribute via σ-type mechanism to the Cu-Cu exchange. This is confirmed by the calculated spin density distribution for the dimer, see Figure 4.

The atomic charges, obtained from the QTAIM partitioning of the experimental and theoretical electron densities of the crystals or the theoretical electron density of the dimeric units, are reported in Table 5S of SI. In all cases, the actual charge of Cu is smaller than the formal oxidation state and the pyrazine is slightly positive, indicating that the σ-donation mechanism is dominating. The halide linkers have a negative charge, though significantly reduced from the formal -1.0, especially for the experimental multipolar model. The BF_4 anion has a charge of ca. -1.0 (with highly positive B and negative F atoms), indicating rather perfect ionic interaction between the cationic $[CuX(pyz)_2]^+$ network and the interstitial BF_4^- anions.

The magnetic structures of **1** and **2** were determined from deuterated powder samples by neutron diffraction in the temperature range from 1.5 K to 15 K. A neutron diffraction pattern of $[CuBr(D_4\text{-}pyz)_2](BF_4)$ measured on DMC with λ = 4.5040 Å at 1.5 K is shown in Figure 5(a) and the magnetic structure in Figure 5(b). The agreement factors for the Rietveld refinement are R_p = 2.9%, R_{wp} = 4.3%, R_{exp} = 0.8%, R_{Bragg} = 1.7%, and R_{mag} = 48.6%. Due to the long wavelength the number of accessible nuclear Bragg peaks was very limited. Therefore, the atomic parameters were fixed to values obtained from 15 K neutron data measured with λ = 3.8040 Å. Upon cooling from 15 K to 1.5 K, weak additional magnetic Bragg peaks appeared below T_N = 3.9(1) K for **1** and 3.8(1) K for **2** which originate from long-range (3D) antiferromagnetic order of the Cu^{2+} spins. For both compounds, the magnetic Bragg peaks are indexed by the propagation vector $\boldsymbol{k}$ = (0,0,0.5); it indicates that the magnetic unit cell is doubled along the *c*-axis with respect to the crystallographic unit cell. Accordingly, the magnetic unit cell contains four Cu^{2+} ions, see Table 5. The best fit of the intensities was obtained for a magnetic structure with ordered moments in the tetragonal plane and AFM coupling both in the *a*-*b* plane and along the *c*-axis, see Figure 5(b). Since the Cu-ligand-Cu angles are 180° along all magnetic exchange paths of the $[CuX(pyz)_2]^+$ framework the observed AFM coupling agrees with theoretical expectations. At 1.5 K the ordered magnetic moments amount to μ_x = 0.76(8) μ_B/Cu^{2+} for **1** and 0.6(1) μ_B/Cu^{2+} for **2**. For uniaxial symmetry, as it is the case for the tetragonal title compounds, neutron powder diffraction data reveal the magnitude of the ordered magnetic moment, its angle with the *c*-axis, and the relative phase between the magnetic ions. The absolute orientation of the ordered moment within the *a*-*b* plane cannot be determined. Therefore, the calculations were done for magnetic moments aligned along the *a*-axis.

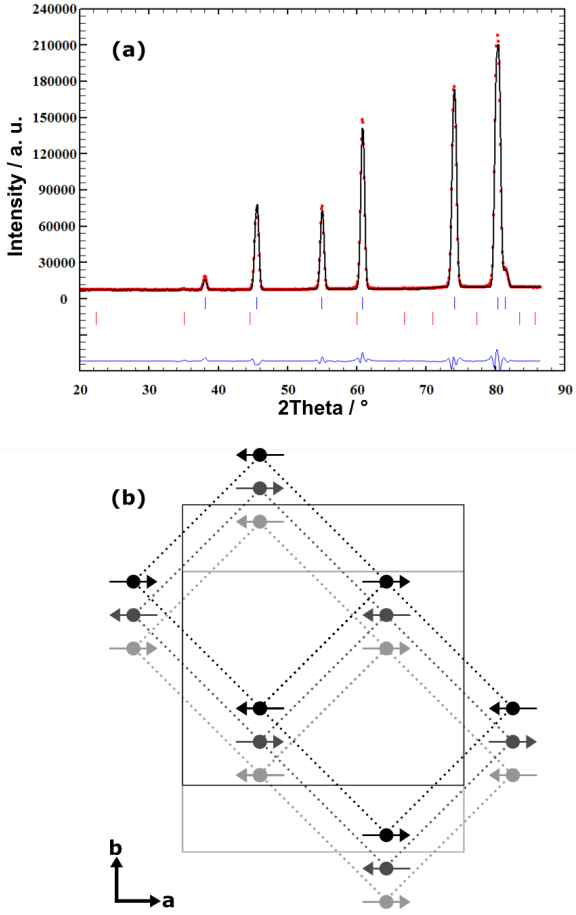

Figure 5. (a) Powder neutron diffraction pattern of $[CuBr(D_4\text{-}pyz)_2](BF_4)$ at 1.5 K (DMC, λ = 4.5040 Å). The graph shows the diffraction pattern (red dots), the Rietveld refinement (black line), the nuclear (blue ticks) and magnetic (red ticks) Bragg positions, and the difference curve (blue line). (b) Magnetic structure with $\boldsymbol{k}$ = (0,0,0.5) in a perspective view along the *c*-axis. Full lines denote the unit cell and dashed lines the Cu^{2+} ion square nets at heights of z/c = 0, 1, and 2.

Table 5. Cu atomic positions in the magnetic unit cell with k = (0,0,0.5) and ordered moments μ_x of $[CuCl(pyz)_2](BF_4)$, 1, and $[CuBr(pyz)_2](BF_4)$, 2, at 1.5 K.

	x/a	y/b	z/c	μ_x/μ_B, **1**	μ_x/μ_B, **2**
Cu1	0.25	0.25	0	0.76(8)	0.6(1)
Cu2	0.75	0.75	0	-0.76	-0.6
Cu3	0.25	0.25	1	-0.76	-0.6
Cu4	0.75	0.75	1	0.76	0.6

$\mu_y = \mu_z = 0\ \mu_B$

For $[CuCl(D_4\text{-}pyz)_2](BF_4)$ a *g*-value of 2.132 was determined from ESR measurements, see below. Accordingly, $g \cdot S$ = 1.07 μ_B/Cu^{2+} is expected for a fully ordered moment. The observed value of 0.76 μ_B/Cu^{2+} is reduced but in good agreement with values of other Cu^{2+} compounds, e.g. $Cu(DCO_2)_2 \cdot 4D_2O$,[41,42] indicating quantum fluctuations below T_N. The magnetic contributions to the neutron diffraction pattern in Figure 5 are rather tiny. This is a result of the small S=1/2 spin of Cu^{2+}, since the magnetic intensity is proportional to the square of the ordered moments. The

tiny intensity manifests in a large R_{mag} = 48.6% value for the magnetic refinement. Nevertheless, the AFM magnetic structure was clearly determined as the best solution with respect to magnetic peak positions and intensities. Calculations for all other spin orientations resulted in R_{mag} > 85% values.

The temperature dependence of the integrated intensity of the strongest magnetic peak (-101) at 35.7° 2θ is shown in Figure 6. A fit to the power law in Eq. 3 yields the Neél temperatures T_N = 3.9(1) K and 3.8(1) K for the chloride and bromide, respectively. The critical exponent β = 0.23 for a 2D Heisenberg magnet was kept fixed in the fits due to the limited number of data points. The determined Neél temperatures are in good agreement with magnetic susceptibility measurements below.

$$I = I_o\,(1\text{-}T/T_N)^{2\beta} \qquad (3)$$

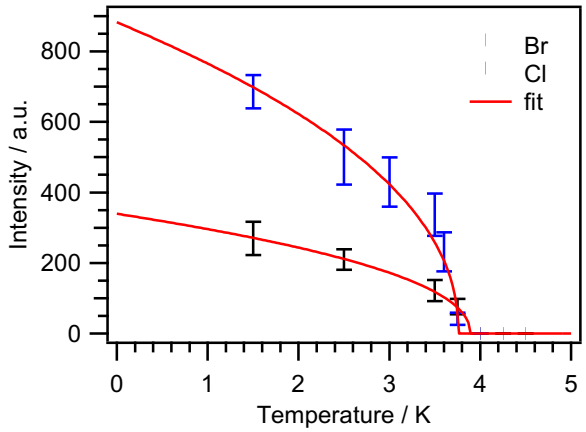

Figure 6. Temperature dependence of the integrated intensity of the (-101) magnetic Bragg peak of **1** (black dots) and **2** (blue dots). Fits to a power law (red lines) result in T_N = 3.9(1) K for **1** and T_N = 3.8(1) K for **2**.

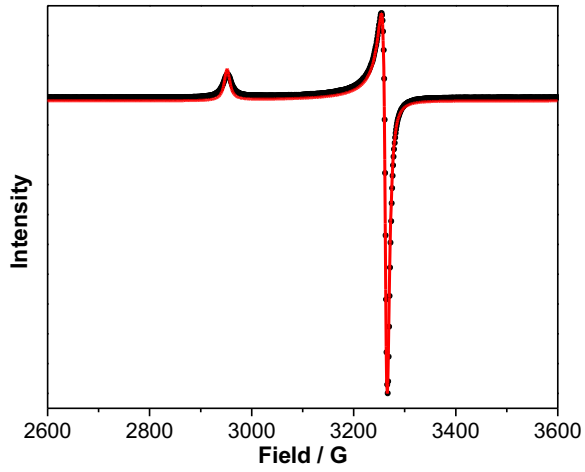

Figure 7. Experimental (black dots) and simulated (red line) X-band ESR spectrum of $[CuCl(D_4\text{-}pyz)_2](BF_4)$ powder. The fit results in g_x = 2.060(1) and g_z = 2.275(1).

The Cu^{2+} g-values and their anisotropy were determined from X-band ESR spectra at room temperature, see Figure 7. For non-deuterated and deuterated $[CuCl(pyz)_2](BF_4)$ powder samples values of g_x = 2.061(1), g_z = 2.276(1) and g_x = 2.060(1), g_z = 2.275(1) were obtained, respectively. Within error limits, the values of the H and D samples are equal. They result in an average g = 2.132(1) for **1**. For the bromide g_x = 2.057(1) and g_z = 2.272(1) were determined with an average g = 2.129(1). The EPR spectra are in perfect agreement with the crystal structure exhibiting a single Cu^{2+} site of axial symmetry, see Table 2S of SI. Similar g values were reported for related $[Cu(pyz)_2]^{2+}$ compounds.[19,34,37,43,44]

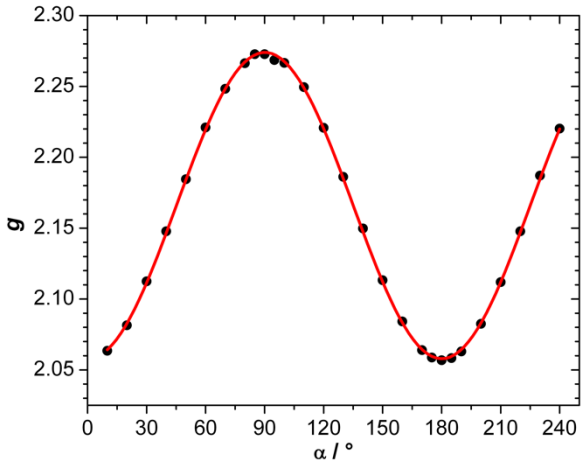

Figure 8. Angular dependence α of the g-value (black dots) of **1** in the a-c plane from single crystal ESR spectra. A sine fit (red line) results in values of g_x = 2.058(1) and g_z = 2.274(1).

The anisotropy of the Cu^{2+} g-value was measured for a non-deuterated single crystal of **1** at room temperature. The tetragonal prismatic crystal had almost equal edges of 1 mm length. Its orientation was verified by X-ray diffraction. Data for a rotation around the b-axis are shown in Figure 8. A sine fit results in values of g_x = 2.058(1) and g_z = 2.274(1). A second data set (not shown here) for the rotation around the c-axis resulted in an isotropic value of g_x = 2.060(1). These single crystal values are in good agreement with powder data. They confirm the axial anisotropy of the g tensor in $[CuX(pyz)_2](BF_4)$ and the $g_x < g_z$ assignment.

The magnetic susceptibility χ and the χ·T product vs. temperature are shown in Figures 9 and 5S of SI, respectively. At 300 K the χ·T values of 0.4139 cm^3K/mol for **1** and 0.4123 cm^3K/mol for **2** were determined. They are in good agreement with the expectation value of $\chi\cdot T = 0.12505\cdot g^2\cdot S\cdot(S+1) = 0.4255\ cm^3K/mol$ with S = 1/2 and g = 2.132 from ESR. The χ·T values decrease with temperature and show a steep decline below 50 K due to antiferromagnetic interactions.

The magnetic susceptibility χ shows a broad maximum around 8 K, see Figure 9. The maximum occurs due to predominantly 2D AFM interactions in the $[Cu(pyz)_2]^{2+}$ planes. According to $J_{||} = 1.07\cdot T_{max}$ an in-plane coupling parameter of $J_{||} \approx 9$ K can be estimated for a 2D Heisenberg system. Data were fitted to a 2D spin ½ Heisenberg model between 4.3 K and 300 K, see Eq. 4.[45] The model includes a small percentage p of paramagnetic impurities with coefficients N_i and D_i from Ref. [45].

$$\chi = \frac{C}{T}\left[1 + \frac{\sum_{i=1}^{5} N_i \left(\frac{J}{k_B T}\right)^i}{1 + \sum_{i=1}^{5} D_i \left(\frac{J}{k_B T}\right)^i}\right](1-p) + \frac{pC}{T}, \quad (4)$$

The fit results in $J_{||}$ = 9.4(1) K for **1** and 8.9 (1) K for **2**, in good agreement with the estimation from T_{max}. The paramagnetic impurities are 1.0(1) % for **1** and 1.3 (1) % for **2**. The expression $g \cdot B_s/J_{||} \approx 6.03\ T$ [4] results in an estimate for the saturation field along the *c*-axis of $B_s \approx 25$ T for **1** and 24 T for **2**. The inter-plane coupling $J_\perp$ is determined by T_N and $J_{||}$. For a quasi-2D Heisenberg antiferromagnet the values are related by Eq. 5,

$$|J_\perp| = J e^{b - 4\pi\rho_s/T_N}, \quad (5)$$

with b = 2.43 and the spin stiffness ρ_s = 0.183 J for a S = ½ system.[46] This results in $|J_\perp|$ = 0.31(6) K for **1** and 0.52(9) K for **2**.

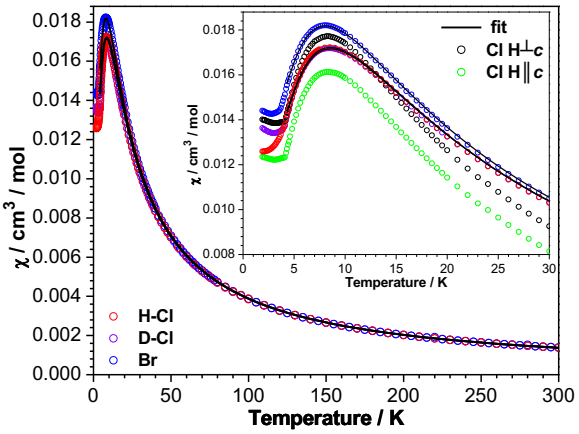

Figure 9. Temperature dependence of the magnetic susceptibility χ for powder samples of non-deuterated **1** (red circles), deuterated **1** (purple circles), and **2** (blue circles). The low temperature part is magnified in the inset, where single crystal data of **1** for $H \| c$ (green circles) and $H \perp c$ (black circles) are added. Fits to a 2D Heisenberg model (black lines) are shown for powder samples of **1** and **2** between 4.3 K and 300 K.

Weak magnetic interactions between the $[Cu(pyz)_2]^{2+}$ layers give rise to 3D order at lower temperature, as proven by neutron diffraction above. The 3D order appears as a kink in the magnetic susceptibility below 4 K, see the inset in Figure 9. The ratios of $T_N/J_{||}$ = 0.41 for **1** and 0.43 for **2** indicate significant interactions between the layers. As for the ESR data, the magnetic susceptibility data for non-deuterated and deuterated samples of **1** were equal within error limits. Only small variations in the paramagnetic impurities were observed between the different samples.

Single crystal susceptibility data of $[CuCl(pyz)_2](BF_4)$ for $H \| c$ and $H \perp c$ coincide from 300 K down to 190 K (data not shown here). Towards lower temperature, see the inset in Figure 9, an anisotropy is observed with higher χ values for $H \perp c$, which is in agreement with the magnetic structure, see Figure 5(b), and ordered moments in the *a*-*b* plane.

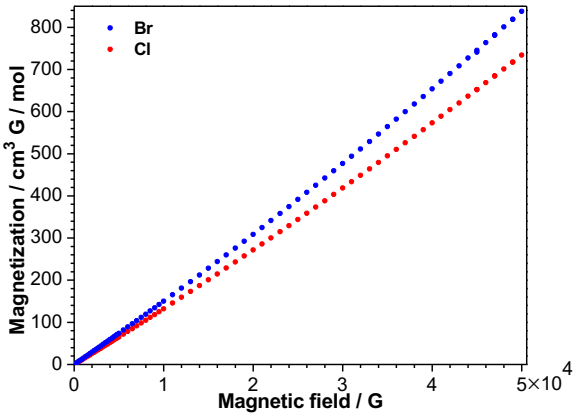

Figure 10. Magnetization of powder samples of **1** (red dots) and **2** (blue dots) at 1.9 K.

Magnetization measurements of **1** and **2** at 1.9 K are shown in Figure 10. The magnetization increases approximately linearly with the magnetic field up to about 1 Tesla. For higher fields the curves show an upturn and rise faster than linear. Such behavior is typical for low-dimensional AFM coupled Cu^{2+} compounds with a low spin (singlet) ground state.[4,18,47,48,49] Increasing magnetic fields flip spins and populate higher spin states (triplets) which results in the upturn of the magnetization. The observed value of 734 cm^3G/mol for **1** at 5 Tesla is far from saturation, where $M = N \cdot \mu_B \cdot g \cdot S$ = 5954 cm^3G/mol is expected for S=1/2 and g = 2.132. The low experimental value at 5 Tesla is in agreement with the much higher estimated saturation field of $B_s \approx 28$ Tesla from the 2D Heisenberg model. A slightly higher magnetization value of 838 cm^3G/mol is observed for **2** at 5 Tesla. It is in agreement with the smaller $J_{||}$ = 8.9 K for the bromide compared to $J_{||}$ = 9.4 K for the chloride.

The aim of the present study is to establish magneto-structural correlations in the $[Cu(pyz)_2]^{2+}$ series by adding two new compounds $[CuX(pyz)_2](BF_4)$ with X = Cl, Br and distinctly shorter Cu-X-Cu distances, see Table 3. For all compounds the Cu-pyz-Cu distances are located in a very narrow range from 6.852 to 6.895 Å. Therefore, the Cu-pyz-Cu distances do not significantly correlate with the magnetic coupling parameters represented by $J_{||}$ (2D) and T_N (3D). In contrast, the pyz rotation angle is quite variable. For longer Cu-X-Cu distances, an increase of the pyz rotation angle is expected in order to reduce the steric hindrance of pyz ligands in the tetragonal plane. Although, this is not valid for **1** and **2**, where the Cu-X-Cu distance is about 0.2 Å longer in **2**, but the pyz rotation angle decreases by more than 3°. In Table 3, the pyrazine rotation angle ranges from about 55° to 90°. As discussed above, the perfectly vertical pyrazines are likely affected by disorder over two conformations. Again no significant correlation is found with the magnetic coupling: for example, in the three BF_4^- salts the pyrazine rotation angle is 55.4°, 58.8°, and 59.4° for X = Br, Cl, and HF_2, respectively, but $J_{||}$ and T_N for the chloride and bromide are much higher than for HF_2^-. This lack of correlation agrees well with the topological analysis of the electron density which reveals that the Cu-N exchange is predominantly σ-type and independent from the pyz rotation angle. Compounds no. 1-4 and 9-10

from Table 3 contain the same $[Cu(HF_2)(pyz)_2]^+$ 3D coordination network. Noteworthy, the magnetic interactions in no. 9-10 are distinctly weaker than for 1-4, despite shorter Cu-X-Cu distances. The contacts between pyz and the interstitial anions have an important influence on the pyz rotation angle, too, and break a clear correlation with the Cu-X-Cu distance. Such observations are not rationalized by present models and ask for further investigation. Present theoretical modelling qualitatively explains the magnetic interactions and their dimensionality.

As a result of this multi-parameter space, it appears that magneto-structural correlations can be established in narrow subsections of the $[Cu(pyz)_2]^{2+}$ family, only. For $[CuX(pyz)_2](BF_4)$ with X = Cl, Br, and (HF_2), cf. no. 6, 7, and 10 in Table 3, $J_{||}$ and T_N are displayed *vs.* the Cu-X-Cu distance in Figure 11. Both $J_{||}$ and T_N decrease with increasing Cu-X-Cu distance. The substitution of Y = BF_4^- by ClO_4^- (no. 9) or X = HF_2^- by NO_2^- (no. 8) increases $J_{||}$ and the correlation is already broken by these small variations. These results call for further measurements and calculations of structural and magnetic properties under pressure that we are currently undertaking in our laboratories. Only the study of the same compound under various external parameters will disentangle the correlation among variables.

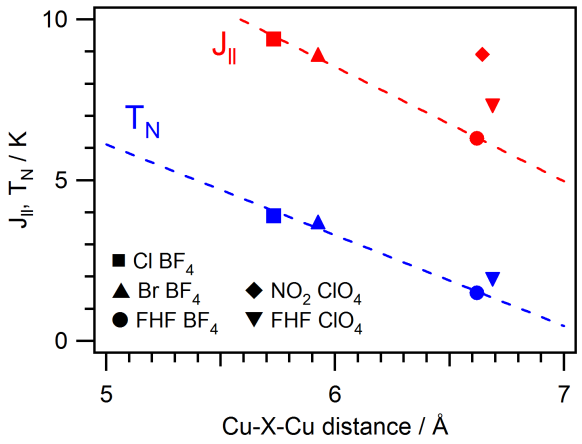

Figure 11. Correlation of $J_{||}$ and T_N with the Cu-X-Cu distance for $[CuX(pyz)_2]Y$ compounds no. 6-10 in Table 3. The dashed lines represent linear fits for compounds with Y = BF_4^-.

CONCLUSIONS

Two new Cu^{2+} coordination polymers $[CuX(pyz)_2](BF_4)$ with X = Cl and Br were synthesized and single crystals grown by controlled evaporation from aqueous solution. The isostructural tetragonal compounds consist of $[Cu(pyz)_2]^{2+}$ layers linked by halide anions X^- into a $[CuX(pyz)_2]^+$ 3D coordination network. The charge is compensated by interstitial BF_4^- anions. The mono-atomic halide linkage is unique among the reported $[Cu(pyz)_2]^{2+}$ compounds and result in distinctly shorter interlayer distances. The 3D coordination network gives rise to low solubility and high thermal stability. Temperature dependent diffraction measurements revealed a pronounced structural anisotropy with rigid Cu-pyz-Cu and much softer Cu-X-Cu linkage. The shorter Cu-N and longer Cu-X bonds of the octahedral Cu^{2+} coordination indicate that the $d_{x^2-y^2}$ magnetic orbital is located in the tetragonal plane. Experimentally and theoretically derived d-orbital occupancies clearly confirm the location of the $d_{x^2-y^2}$ orbital in the *a*-*b* plane. These materials are very important for their magnetic properties, which were characterized by neutron diffraction, magnetic susceptibility, and ESR measurements. The Cu^{2+} *g*-tensor is close to isotropic with a 10% larger g_z value at room temperature. The χ vs. T curves show a broad maximum below 10 K characteristic for a 2D Heisenberg antiferromagnet. The intralayer interactions $J_{||}$ are much stronger than magnetic interactions between the $[Cu(pyz)_2]^{2+}$ layers. Below 4 K 3D antiferromagnetic order sets in and moments are localized in the tetragonal plane. Some open questions remain concerning the correlation of structural and magnetic properties in $[CuX(pyz)_2]Y$ compounds, that may depend on multiple parameters. The rigidity of the Cu-pyz-Cu linkage implies no correlation with $J_{||}$ and T_N. On the contrary, the rotation of pyrazine about the Cu-N axis is quite variable and strongly depends on Y anions. However, the σ-type Cu-N exchange mechanism is necessarily independent on the pyz rotation angle. The electronic polarizability of the X linker appears less important, otherwise a higher T_N would be expected for the bromide. Magneto-structural correlations may be drawn for narrow subsections only, as discussed for $[CuX(pyz)_2](BF_4)$ with X = Cl, Br, and (HF_2). This fosters further investigations that are currently in due course in our laboratories. In particular, given the soft nature of the Cu-X-Cu interlayer connection, we expect a significant increase of the ratio between magnetic interactions $J_\perp/J_{||}$ upon application of isotropic external pressure. Moreover, further chemical variations of ligands and counter anions will provide a wider data basis which is required for more systematic analyses of correlations between structural features and magnetic exchange.

ASSOCIATED CONTENT

Supporting Information. TG curves, FTIR spectrum, powder X-ray diffraction data at RT, 5 K, and neutron diffraction data at 1.5 K, temperature dependent lattice parameters, atomic positions and displacement parameters from single crystal data, Table of compounds with distorted $[Cu(pyz)_2]^{2+}$ layers, details on multipole model refinements, bond critical properties, and atomic charges, ESR spectrum, and magnetic susceptibility χ·T vs. T. (PDF)
Crystal data. (CIF)
This material is available free of charge via the Internet at http://pubs.acs.org.

AUTHOR INFORMATION

Corresponding Authors

*piero.macchi@dcb.unibe.ch
*christian.rueegg@psi.ch
*karl.kraemer@dcb.unibe.ch

Notes

The authors declare no competing financial interest.

ACKNOWLEDGMENT

Part of this work is based on experiments performed at the Swiss spallation neutron source (SINQ) and the Swiss Light

Source (SLS), Paul Scherrer Institute (PSI), Villigen, Switzerland. MK and BW acknowledge funding from the European Community's Seventh Framework Program (FP7/2007-2013) under Grant Agreement No. 290605 (PSIFELLOW/COFUND). The research leading to these results has received funding from the Swiss National Science Foundation under grant no. 200020_150257 and 200020_160157.

[1] Vaknin, D.; Sinha, S. K.; Moncton, D. E.; Johnston, D. C.; Newsam, J. M.; Safinya, C. R.; King, H. E. *Phys. Rev. Lett.* **1987**, *58*, 2802–2805.

[2] Tranquada, J.; Cox, D.; Kunnmann, W.; Moudden, H.; Shirane, G.; Suenaga, M.; Zolliker, P.; Vaknin, D.; Sinha, S.; Alvarez, M.; Jacobson, A.; Johnston, D. *Phys. Rev. Lett.* **1988**, *60*, 156–159.

[3] Bednorz, J. G.; Müller, K. A. *Z. Phys. B - Condens. Matter* **1986**, *64*, 189–193.

[4] Goddard, P. A.; Singleton, J.; Sengupta, P.; McDonald, R. D.; Lancaster, T.; Blundell, S. J.; Pratt, F. L.; Cox, S.; Harrison, N.; Manson, J. L.; Southerland, H. I.; Schlueter, J. A. *New J. Phys.* **2008**, *10*, 083025.

[5] Christensen, N. B.; Rønnow, H. M.; McMorrow, D. F.; Harrison, A.; Perring, T. G.; Enderle, M.; Coldea, R.; Regnault, L. P.; Aeppli, G. *Proc. Natl Acad. Sci.* **2007**, *104*, 15264–15269.

[6] Dalla Piazza, B.; Mourigal, M.; Christensen, N. B.; Nilsen, G. J.; Tregenna-Piggott, P.; Perring, T. G.; Enderle, M.; McMorrow, D. F.; Ivanov, D. A.; Ronnow, H. M. *Nat. Phys.* **2015**, *11*, 62–68.

[7] Carlin, R. L. Magnetochemistry; Springer Berlin, 1986.

[8] Day, P.; Underhill, A. E. Metal-Organic and Organic Molecular Magnets; The Royal Society of Chemistry, London, 1999.

[9] Bartolomé, J.; Luis, F.; Fernández, J. F. Molecular Magnets Physics and Applications; Springer-Verlag Berlin Heidelberg 2014.

[10] Hong, M.; Chen, L. Design and Construction of Coordination Polymers; Wiley, Inc., Hoboken, New Jersey, 2009.

[11] Turnbull, M. M.; Sugimoto, T.; Thompson, L. K. Molecule-Based Magnetic Materials; American Chemical Society, Washington, DC, 1996.

[12] Willett, R. D.; Landee, C.; Swank, D. D. *J. Appl. Phys.* **1978**, *49*, 1329–1330.

[13] Manson, J. L.; Conner, M. M.; Schlueter, J. A.; Mcconnell, A. C.; Southerland, H. I.; Malfant, I.; Lancaster, T.; Blundell, S. J.; Brooks, M. L.; Pratt, F. L.; Singleton, J.; Mcdonald, R. D.; Lee, C.; Whangbo, M. *Chem. Mater.* **2008**, *20*, 7408–7416.

[14] Lanza, A.; Fiolka, C.; Fisch, M.; Casati, N.; Skoulatos, M.; Rüegg, C.; Krämer, K. W.; Macchi, P. *Chem. Commun.* **2014**, *50*, 14504–14507.

[15] Nath, R.; Padmanabhan, M.; Baby, S.; Thirumurugan, A.; Tsirlin, A. A. *Phys. Rev. B* **2015**, *91*, 054409.

[16] Woodward, F. M.; Gibson, P. J.; Jameson, G. B.; Landee, C. P.; Turnbull, M. M.; Willett, R. D. *Inorg. Chem.* **2007**, *46*, 4256–4266.

[17] Brown, S.; Cao, J.; Musfeldt, J. L.; Conner, M. M.; McConnell, A. C.; Southerland, H. I.; Manson, J. L.; Schlueter, J. A.; Phillips, M. D.; Turnbull, M. M.; Landee, C. P. *Inorg. Chem.* **2007**, *46*, 8577–8583.

[18] Manson, J. L.; Schlueter, J. A.; Funk, K. A.; Southerland, H. I.; Twamley, B.; Lancaster, T.; Blundell, S. J.; Baker, P. J.; Pratt, F. L.; Singleton, J.; Mcdonald, R. D.; Goddard, P. A.; Sengupta, P.; Batista, C. D.; Ding, L.; Lee, C.; Whangbo, M.-H.; Franke, I.; Cox, S.; Baines, C.; Trial, D. *J. Am. Chem. Soc.* **2009**, *131*, 6733–6747.

[19] Manson, J. L.; Schlueter, J. A.; McDonald, R. D.; Singleton, J. *J. Low Temp. Phys.* **2010**, *159*, 15–19.

[20] Macchi, P.; Bürgi, H.-B.; Chimpri, A. S.; Hauser, J.; Gál, Z. *J. Appl. Cryst.* **2011**, *44*, 763–771.

[21] CrysAlisPro (Version 171.36.28). 2010.

[22] Sheldrick, G. M. *Acta Cryst. C.* **2008**, *64*, 112–122.

[23] Hansen, N. K.; Coppens, P. *Acta Cryst. A.* **1978**, *34*, 909–921.

[24] Volkov, A.; Macchi, P.; Farrugia, L. J.; Gatti, C.; Mallinson, P.; Richter, T.; Koritsanszky, T. XD2015. 2015.

[25] Holladay, A.; Leung, P.; Coppens, P. *Acta Cryst. A.* **1983**, *39*, 377–387.

[26] Willmott, P. R.; Meister, D.; Leake, S. J.; Lange, M.; Bergamaschi, A.; Böge, M.; Calvi, M.; Cancellieri, C.; Casati, N.; Cervellino, A.; Chen, Q.; David, C.; Flechsig, U.; Gozzo, F.; Henrich, B.; Jäggi-Spielmann, S.; Jakob, B.; Kalichava, I.; Karvinen, P.; Krempasky, J.; Lüdeke, A.; Lüscher, R.; Maag, S.; Quitmann, C.; Reinle-Schmitt, M. L.; Schmidt, T.; Schmitt, B.; Streun, A.; Vartiainen, I.; Vitins, M.; Wang, X.; Wullschleger, R. *J. Synchrotron Rad.* **2013**, *20*, 667–682.

[27] Coelho, A. A. (2012). TOPAS Academic. Version 5. Coelho Software, Brisbane, Australia.

[28] Fischer, P.; Keller, L.; Schefer, J.; Kohlbrecher, J. *Neutron News* **2000**, *11*, 19–21.

[29] Roisnel, T.; Rodriguez-Carvajal, J. *WinPLOTR: A Windows Tool for Powder Diffraction Pattern Analysis. Paper Presented at the Proceedings of the Seventh European Powder Diffraction Conference (EPDIC 7)*; 2000.

[30] Rodriguez-Carvajal, J. *Phys. B* **1993**, *192*, 55–69.

[31] Dovesi, R.; Saunders, V. R.; Roetti, C.; Orlando, R.; Zicovich-Wilson, C. M.; Pascale, F.; Civalleri, B.; Doll, K.; Harrison, N. M.; Bush, I. J.; D'Arco, P.; Llunell, M.; Causà, M.; Noël, Y. CRYSTAL14 User's Manual. University of Torino: Torino 2014.

[32] Doll, K.; Harrison, N. M. Chlorine *Chem. Phys. Lett.* **2000**, *317*, 282–289.

[33] Peintinger, M. F.; Oliveira, D. V.; Bredow, T. *J. Comp. Chem.* **2013**, *34*, 451–459.

[34] Frisch, M. J.; Trucks, G. W.; Schlegel, H. B.; Scuseria, G. E.; Robb, M. A.; Cheeseman, J. R.; Scalmani, G.; Barone, V.; Mennucci, B.; G. A. Petersson, H. N.; Caricato, M.; Li, X.; Hratchian, H. P.; Izmaylov, A. F.; Bloino, J.; Zheng, G.; Sonnenberg, J. L.; Hada, M.; Ehara, M.; Toyota, K.; Fukuda, R.; Hasegawa, J.; Ishida, M.; Nakajima, T.; Honda, Y.; Kitao, O.; Nakai, H.; Vreven; Montgomery, T.; Jr., J. A.; Peralta, J. E.; Ogliaro, F.; Bearpark, M.; Heyd, J. J.; Brothers, E.; Kudin, K. N.; Staroverov, V. N.; Kobayashi, R.; Normand, J.; Raghavachari, K.; Rendell, A.; Burant, J. C.; Iyengar, S. S.; Tomasi, J.; Cossi, M.; Rega, N.; Millam, J. M.; Klene, M.; Knox, J. E.; Cross, J. B.; Bakken, V.; Adamo, C.; Jaramillo, J.; Gomperts, R.; Stratmann, R. E.; Yazyev, O.; Austin, A. J.; Cammi, R.; Pomelli, C.; Ochterski, J. W.; Martin, R. L.; Morokuma, K.; Zakrzewski, V. G.; Voth, G. A.; Salvador, P.; Dannenberg, J. J.; Dapprich, S.; Daniels, A. D.; Farkas, Ö.; Foresman, J. B.; Ortiz, J. V.; Cioslowski, J.; Fox, D. J. Gaussian 09. Gaussian, Inc.: Wallingford, CT 2009.

[35] Cizmar, E.; Zvyagin, S. A.; Beyer, R.; Uhlarz, M.; Ozerov, M.; Skourski, Y.; Manson, J. L.; Schlueter, J. A.; Wosnitza, J. *Phys. Rev. B.* **2010**, *81*, 064422–064425.

[36] Lancaster, T.; Blundell, S.; Baker, P.; Brooks, M.; Hayes, W.; Pratt, F.; Manson, J.; Conner, M.; Schlueter, J. *Phys. Rev. Lett.* **2007**, *99*, 267601–267604.

[37] Liu, T.; Chen, Y.-H.; Zhang, Y.-J.; Wang, Z.-M.; Gao, S. *Inorg. Chem.* **2006**, *45*, 9148–9150.

[38] Manson, J. L.; Conner, M. M.; Schlueter, J. A.; Lancaster, T.; Blundell, S. J.; Brooks, M. L.; Pratt, F. L.; Papageorgiou, T.; Bianchi, A. D.; Wosnitza, J.; Whangbo, M.-H. *Chem. Commun.* **2006**, *4*, 4894–4896.

[39] Santos, L. H. R. Dos; Lanza, A.; Barton, A. M.; Brambleby, J.; Blackmore, W. J. A.; Paul, A.; Xiao, F.; Williams, R. C.; Lancaster, T.; Pratt, F. L.; Blundell, S. J.; Singleton, J.; Manson, L.; Macchi, P. *J. Am. Chem. Soc.* **2016**, *138*, 2280–2291.

[40] Bader, R. W. F. A Quantum Theory; Oxford University Press, 1990.
[41] Clarke, S. J.; Harrison, A.; Mason, T. E.; McIntyre, G. J.; Visser, D; *J. Phys. Condens. Matter* **1992**, *4*, L71–L76.
[42] Taroni, A.; Bramwell, S. T.; Holdsworth, P. C. W. *J. Phys. Condens. Matter* **2008**, *20*, 275233.
[43] Sengupta, P.; Batista, C. D.; McDonald, R. D.; Cox, S.; Singleton, J.; Huang, L.; Papageorgiou, T. P.; Ignatchik, O.; Herrmannsdörfer, T.; Manson, J. L.; Schlueter, J. A.; Funk, K. A.; Wosnitza, J. *Phys. Rev. B.* **2009**, *79*, 060409(R).
[44] Manson, J. L.; Lapidus, S. H.; Stephens, P. W.; Peterson, P. K.; Carreiro, K. E.; Southerland, H. I.; Lancaster, T.; Blundell, S. J.; Steele, A. J.; Goddard, P. A.; Pratt, F. L.; Singleton, J.; Kohama, Y.; McDonald, R. D.; Del Sesto, R. E.; Smith, N. A.; Bendix, J.; Zvyagin, S. A.; Kang, J.; Lee, C.; Whangbo, M.-H.; Zapf, V. S.; Plonczak, A. *Inorg. Chem.* **2011**, *50*, 5990–6009.
[45] Landee, C. P.; Turnbull, M. M. *J. Coord. Chem.* **2014**, *67*, 375–439.
[46] Yasuda, C.; Todo, S.; Hukushima, K.; Alet, F.; Keller, M.; Troyer, M.; Takayama, H. *Phys. Rev. Lett.* **2005**, *94*, 217201.
[47] Woodward, F. M.; Albrecht, A. S.; Wynn, C. M.; Landee, C. P.; Turnbull, M. M. *Phys. Rev. B* **2002**, *65*, 144412.
[48] Matsumoto, T.; Miyazaki, Y.; Albrecht, A. S.; Landee, C. P.; Turnbull, M. M.; Sorai, M. *J. Phys. Chem. B* **2000**, *104*, 9993–10000.
[49] Day, P. Electronic Structure and Magnetism of Inorganic Compounds; The Chemical Society, Great Britain, 1977; Vol. 5.